Accepted Manuscript

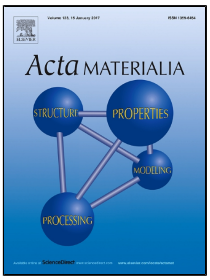

Cohesive and adhesive properties of ultrathin amorphous and crystalline $Ge_2Sb_2Te_5$ films on polyimide substrates

Franziska F. Schlich, Andreas Wyss, Henning Galinski, Ralph Spolenak

PII:	S1359-6454(16)31008-4
DOI:	10.1016/j.actamat.2016.12.060
Reference:	AM 13448
To appear in:	*Acta Materialia*
Received Date:	06 July 2016
Revised Date:	17 December 2016
Accepted Date:	24 December 2016

Please cite this article as: Franziska F. Schlich, Andreas Wyss, Henning Galinski, Ralph Spolenak, Cohesive and adhesive properties of ultrathin amorphous and crystalline $Ge_2Sb_2Te_5$ films on polyimide substrates, *Acta Materialia* (2016), doi: 10.1016/j.actamat.2016.12.060

Cohesive and adhesive properties of ultrathin amorphous and crystalline $Ge_2Sb_2Te_5$ films on polyimide substrates

Franziska F. Schlich[a], Andreas Wyss[a], Henning Galinski[a], Ralph Spolenak[a]*

[a]Laboratory for Nanometallurgy, Department of Materials, ETH Zürich, Vladimir-Prelog-Weg 5, 8093 Zürich, Switzerland

*E-mail: ralph.spolenak@mat.ethz.ch

Abstract

In this work, the onset strains of fragmentation, the fracture strength, and fracture toughness of amorphous and crystalline $Ge_2Sb_2Te_5$ (GST) films are determined. Using *in situ* methods, such as resistance measurements, reflectance anisotropy spectroscopy (RAS), and ~~optical~~ light microscopy during uniaxial tensile loading, we demonstrate that onset strain of fragmentation and delamination depend on both, crystallographic state of the GST film and the film thickness. We observe that amorphous GST fractures at larger strains than crystalline GST. However, due to its small Young's modulus the fracture toughness K_{IC} of amorphous GST is lower than that of crystalline GST (amorphous: $K_{IC} = 0.4 \pm 0.2$ MPa m$^{0.5}$; crystalline: $K_{IC} = 0.8 \pm 0.2$ MPa m$^{0.5}$). The results presented are critically discussed with respect to the potential application of GST films in flexible displays.

Keywords: optical spectroscopy, mechanical behavior, thin films, phase transformation

1. Introduction

Phase change materials (PCMs) are typically two-state systems, whose physical properties can be changed reversibly upon an external stimulus. Some prominent examples are chalcogenide glasses which can be switched reversibly and rapidly between their amorphous and crystalline phase upon heating [1]. The chemical bonding mechanisms in the two phases differ significantly which yields in a 70 – 200 % larger optical dielectric constant for the crystalline phase [2]. The resulting prominent optical and electrical contrast between both phases is exploited in rewritable optical data storage [3], non-volatile electronic memories [4], and offers great potential for tunable nanophotonic components [5]. Moreover, it has been demonstrated recently, that the phase-change material $Ge_2Sb_2Te_5$ (GST) is a promising candidate for non-volatile display [6, 7] and data visualization applications [6]. Using thin GST films in the nanometer range and transparent electrodes enable electrically induced color changes upon phase change on both, rigid and flexible substrates.

Although phase-change materials have extraordinary properties some challenges still remain. The density increase upon crystallization manifests itself in a thickness decrease, because the coating is well adhered to its substrate. ~~large thickness decrease as t upon crystallization which~~ For GST this thickness decrease is 6.5 % [8] ~~for GST~~ and leads to a pronounced mechanical stress and might result in cracks in the film. Atomic force microscopy measurements of laser-induced crystallized GST for example show cracks in the crystalline region for laser pulses in the ns-µs range [9]. Another failure mechanism which applies to display applications on flexible substrates is bending or straining of the substrate which might induce cracks in the GST film.

Consequently, in the following we focus on determining the mechanical properties of GST films, especially at film thicknesses relevant for the application. In literature, most researchers focused on the investigation of Young's moduli of amorphous, metastable cubic, and stable hexagonal GST. Various methods such as wafer curvature [8], nanoindentation [10], microtensile measurements [11], and micromechanical resonating beams [12] were applied. Young's moduli between 10 GPa and 25 GPa for amorphous GST and values between 25 GPa and 60 GPa for crystalline GST were obtained [8, 10-12] depending on the method, the film thickness, and the annealing temperature. Choi *et al.* [11] performed uniaxial microtensile tests of 500 nm amorphous GST and investigated the average crack spacing in the film as a function of strain. They determined an onset strain of fragmentation of 0.6 %. However, no analysis of the crack evolution was carried out and only one film thickness and no crystalline GST was characterized.

In the present work, we overcome this gap by investigating the cohesive and adhesive properties of amorphous and crystalline GST films in the thickness range from 20 nm to 400 nm. Various *in situ* methods such as ~~optical~~ light microscopy, resistance measurements, and reflectance anisotropy spectroscopy (RAS) are applied during uniaxial loading of the samples to determine the onset strain of fragmentation and delamination, the fracture strength, and the fracture toughness. RAS measures the normalized difference in reflectance of linearly polarized light between two perpendicular directions (x, y) in the surface plane [13]:

$$\frac{\Delta r}{r} = 2\frac{r_x - r_y}{r_x + r_y} \quad (1)$$

Note that the reflection coefficients *r* are complex numbers. This method is amongst others applied to monitor the growth of semiconductors [14], to determine the adsorption on surfaces [15], or to characterize the mechanical properties of a material [16-18].

In addition, we demonstrate that RAS can be applied to determine the onset strain of fragmentation of brittle films. Cracks in the film occur perpendicular to the loading direction and consequently, result in an anisotropy in the reflectance of polarized light parallel and orthogonal to the strain direction.

2. Experimental details

GST films of 20 nm, 30 nm, 50 nm, 100 nm, 200 nm, and 400 nm were produced by direct current magnetron sputtering (PVD Products) using a power of 20 W. The background pressure in the chamber was better than $8 \cdot 10^{-5}$ Pa and during the depositions, an Ar flow of 20 sccm and a pressure of 0.67 Pa were used. In order to achieve homogeneous film thicknesses the substrate was rotated with 30 rpm. The polyimide substrates Kapton® E from DuPont with a thickness of 50 µm were cleaned in acetone and isopropanol and baked in a furnace for at least 6 h at 200 °C prior to deposition.

Raman measurements were performed with a green laser at 532 nm. The laser intensity was reduced to 0.16 mW/µm^2 to avoid laser-induced crystallization of the sample. Crystallization was performed under Ar atmosphere in a furnace. The samples were annealed at 200-210 °C for 6 min with a heating rate of 30 °C/min. The phase transition to the cubic phase is at around 160 °C for

250 nm thick films for heating rates of 30 °C/min [19]. XRD was carried out to analyze the crystalline structure. A θ-2θ scan from 3° to 120° was performed with a step size of 0.008°.

The residual stress σ_{res} of the films was determined by measuring the curvature of the polyimide substrates with the GST films by ~~optical~~ light microscopy and calculating σ_{res} using Stoney's equation [20]. For uniaxial tensile tests, the samples were mounted into a tensile machine (Kammrath & Weiss GmbH). Each sample was 5 mm wide and the strain rates were $5.3 \cdot 10^{-5}$ s^{-1} (~~optical~~ light microscopy and RAS measurement) and $1.1 \cdot 10^{-4}$ s^{-1} (resistance measurements). *In situ* confocal light microscopy (WITec CRM200) was performed with a 100x objective to observe the crack patterns during stepwise loading. The mean crack distance $\overline{L}$ was calculated with a Matlab routine [21]. The analysis of the crack evolution leads to fracture strength σ_f and fracture toughness K_{IC} values of the GST layers.

An electrical resistance module was used in a constant current mode to record the change of the normalized resistance R/R_0 with the initial resistance R_0 of all films during uniaxial loading. The current was minimized (100 mA) to prevent heating of the sample and the change of voltage was recorded. Due to its low specific resistance, the resistance change of amorphous GST was monitored indirectly by measuring the resistance of a conductive Pt capping layer during loading. Hence, GST films with a 3 nm Pt capping layer were sputtered without breaking the vacuum in between. A direct current power of 41 W, a pressure of 0.67 Pa, and an Ar flow of 20 sccm were used for Pt deposition.

Reflectance anisotropy spectra were measured with a photoelastic modulator (PEM) based RAS-setup [22] designed and fabricated at the Institute of Experimental Physics, JKU Linz. The spectra were recorded in an energy range from 1.5 to 5.5 eV in intervals of 0.02 eV and with an integration

time of 1 s per energy step. The spot size at the sample surface was 2 mm and the loading direction of the tensile machine was set in x-direction in Equation 1. The RAS data was recorded during continuous loading at a single photon energy of the sample to track the evolution of one feature. Alternatively, data was obtained stepwise which means a whole spectrum in the range from 1.5 to 5.5 eV was acquired while straining was briefly interrupted. For all RAS measurements the Kapton® E substrates were roughened on the back by abrasive paper to prevent a reflection from this surface.

3. Results

3.1 Phase analysis

All GST films were amorphous as-deposited as confirmed by Raman spectroscopy (see Figure 1 (b)). To choose the correct Young's modulus of crystalline GST from literature the phase of a 400 nm oven-annealed GST film was investigated by an XRD measurement (see Figure 1 (a)). Reflections of the cubic fcc structure were clearly identifiable and a lattice constant of a=6.00 Å was determined which is consistent with literature [23]. A peak fit of hexagonal reflections was not feasible as hexagonal and trigonal phases were neither distinguishable by the angular position nor by the peak intensity.

3.2 Residual stress

The determined residual stresses of all films are summarized in Table 1. The residual stress is tensile and decreases as a function of film thickness. Crystalline GST films exhibit larger residual stresses than amorphous films because of both, an increase in the Young's modulus ~~increases~~ and densification ~~of the density increase of~~ upon crystallization [8, 10-12]. This increase ~~may be related to the density increase but can also depend on other factors such as anisotropy~~ arises due to the substrate constraint during phase transformation. The Young's modulus of GST

depends on the phase and thickness of the film [12]. Hence, for the calculations we do not use a single Young's modulus value but a range of Young's moduli E_f for the amorphous and crystalline GST films (E_f =10-20 GPa for amorphous GST and E_f = 30-40 GPa for crystalline GST) which is consistent with literature [8, 10-12]. Calculating the elastic strain values from the measured residual stress in the linear elastic regime yields unreasonably high values for ultrathin films below 50 nm. Hence, the validation method for these ultrathin films is ~~questioned~~ questionable and is not used for the calculations in the following for the thinnest layers.

Table 1: Residual stress σ_{res} of amorphous and crystalline GST layers with film thickness d on Kapton® E substrates.

Film thickness d (nm)	σ_{res} amorphous (GPa)	σ_{res} crystalline (GPa)
20	0.78 ± 0.25	1.13 ± 0.36
30	0.57 ± 0.18	0.68 ± 0.20
50	0.30 ± 0.10	0.32 ± 0.10
100	0.15 ± 0.05	0.16 ± 0.05
200	0.08 ± 0.02	0.12 ± 0.04
400	0.05 ± 0.02	0.09 ± 0.03

3.3 Cohesive and adhesive properties

Typical crack patterns of amorphous and crystalline GST at 4 % and 18 % strain are depicted in Figure 2 (a) and (b). Cracks in the crystalline film (b) deviate from straight paths as they have to propagate ~~through~~ along the grain boundaries in contrast to those in amorphous GST (a). Generally, buckling was not observed for amorphous GST up to strain values of 20 % while crystalline films show delamination as presented in the lower micrograph of Figure 1 (b).

Figure 2 (c) and (d) report the normalized resistance curves as a function of strain. Typical resistance measurements are compared to the ideal plastic deformation curve [16, 24]. As GST does not exhibit plastic deformation, here the change of resistance is calculated as a function of

uniaxial strain. For this ideal resistance change $\frac{R}{R_0} = (1+\varepsilon)(1+2\nu_f\varepsilon)$ (black line) the Poisson's ratio of the film (ν_f=0.3 [25]) and the applied uniaxial strain ε need to be considered. A 5 % deviation of this ideal resistance change is typically a reliable measure for first cracks in the films (dashed black line) [24]. The resistance of amorphous GST, which is less conductive than crystalline GST (amorphous: (3-6)·10^3 Ωcm; cubic: (1-4))·10^{-1} Ωcm [26]), was measured indirectly by a thin conductive Pt capping layer. First cracks in a single Pt film occur at around 3 % strain which is indicated by the intersection of the resistance curve (gray line) with the 5 % deviation from the ideal resistance change (black dashed line) as can be seen in Figure 2 (c). A deviation from the ideal resistance curve appears for amorphous GST films at lower strain values which demonstrates that first cracks occur in amorphous GST and not in the Pt top layer. The resistance curves of amorphous GST films dramatically increase as soon as they deviate from the ideal behavior which reveals that a crack propagates immediately through the whole film as soon as it appears. For 50 nm amorphous GST the slope of the normalized resistance is less steep. It might be that the crack opening of this thin film is too small to instantly induce a crack in the Pt film which propagates immediately through the whole film. Consequently, the determined onset strain of fragmentation of 50 nm amorphous GST might be overestimated and measurements of even thinner amorphous GST films with Pt capping layers are not reliable.

The slope of the normalized resistance curves of crystalline GST films (see Figure 2 (d)) deviate from the ideal resistance change as soon as the films are strained. At low strains the slopes of the normalized resistance curves are the same for all crystalline GST films. This slope further increases at a strain value depending on the film thickness. The deviation from the ideal behavior may have two possible origins: On the one hand, crystalline films may exhibit small cracks which start to

open as soon as the film is loaded. At higher strain values the slope of the normalized resistance further increases due to new cracks which occur in the film. On the other hand, straining of the crystalline films may result in changes of the electronic structure which is in analogy to semiconductors such as Si or Ge [27]. A resulting shift in the energy levels may induce a piezoresistive effect [28]. The first case can be discarded as the curves are perfectly reversible upon loading and unloading at low strain values as presented for 30 nm crystalline GST. A deviation from the initial resistance slope indicates the formation of first cracks such that these strain values are taken as onset strains of fragmentation. ~~Exemplarily,~~ Typical scattering in data is demonstrated for 100 nm crystalline GST ~~scattering in data is demonstrated~~ by an error bar which results from three different resistance measurements. Generally, the onset strain of fragmentation decreases as a function of film thickness for amorphous and crystalline GST films.

Characteristic formations of crack patterns are obtained upon uniaxial tensile loading of thin brittle films. In Figure 2 the mean crack distances as a function of applied strain are presented for amorphous (e) and crystalline (f) thin films. The mean crack distance versus strain curves can be divided into three regimes [29] as ~~exemplarily~~ shown for ~~the~~ a typical crack evolution of 100 nm amorphous GST. From the first defect-controlled regime the fracture strength of the coating can be calculated from fragmentation kinetics. At the crossover length L_c cracks occur mainly in the center of a fragment as stress relaxation zones start to overlap. At high strains ε_{sat} no further cracks occur due to substrate yielding. Cracks in very thin films (20 nm and 30 nm) cannot be observed by ~~optical~~ light microscopy or *in situ* AFM as the crack openings are too small. Generally, the onset strain of fragmentation determined by ~~optical~~ light microscopy decreases as a function of film thickness.

Figure 3 presents ~~exemplarily~~ typical RA spectra of 100 nm amorphous (a) and crystalline (b) GST films at various strain values. For the unstrained state (0.00 % strain) the real part of the anisotropy signal is zero for all photon energies. For both, amorphous and crystalline GST films, a feature at 2.80 eV appears upon loading which is called the crack feature in the following. The crack feature appears at low strain values (around 1 % strain) and its amplitude increases with increasing strain (see Figure 3 (a), (b) and (f)). Loading of crystalline GST films leads to another feature at 5.06 eV. At low strain values the amplitude of the feature increases and it decreases as soon as the crack feature appears (see Figure 3 (g)). This feature at 5.06 eV is called the elastic feature in the following because it is perfectly reversible upon loading and unloading at strain values below the onset strain of the crack feature (see Figure 3 (g)). The spectral position of the elastic feature does not depend on the film thickness which indicates that it is a material property. In contrast to that, the spectral position of the crack feature depends on the film thickness of the GST layers as can be seen in Figure 3 (c). Here, the measured real part of the anisotropy signal as a function of photon energy is presented for 50 nm, 100 nm, and 400 nm amorphous GST at 5 % strain.

The altered optical response in the RA spectra can be explained as follows: Crack formation in the film always appears perpendicular to the loading direction. The cracks are equidistant and introduce a periodic array of slits, which acts as an optical grating. The grating period, here the mean crack distance, is comparable or larger than the used optical wavelength, whereas the slit width, typically 80 nm, is highly subwavelength. We anticipate that the presence of an optical grating adds an additional component to the polarization dependent response of the measured RA signal.

In order to verify this statement, a series of finite-element simulations (COMSOL™ Multiphysics 5.2) ~~has~~ have been realized, where a model has been build~~t~~ that matches the experimental situation of 50 nm, 100 nm, and 400 nm thick GST based nano-slit arrays with a grating period (crack distances) of 970 nm and slit opening (crack openings) of 80 nm (see Figure 3 (e)). Figure 3 (d) reports the RA spectra calculated from the FE simulations using Equation (1).

Here, only the film thickness acts as critical coupling parameter of the light with constant crack opening and crack distance. The spectral position of the crack feature is in good agreement for measurement and simulation. With increasing film thickness the crack feature shifts to smaller photon energies. However, the exact shape of the spectra differ for measurement and simulation. The simulation assumes a perfect periodic grating but in reality crack openings and crack distances vary. Consequently, the measurement averages grating structures with slightly different periodicity which explains why the spectra are smoother than those of the simulations.

4. Discussion

4.1 Residual stress

The residual stresses of crystalline GST films are more tensile than those of amorphous GST films because of the larger Young's moduli of crystalline films compared to those of amorphous layers and the densification while being constrained by the substrate during phase transformation. ~~density increase upon crystallization.~~ This trend was also observed by Pedersen *et al.* [8]. The intrinsic tensile stress in the amorphous phase is formed during the fabrication process and might be caused by the working gas pressure during sputter deposition [30]. The thickness-dependent trend of the residual stress shown here is probably related to coalescence of islands and atomic peening of the film during sputter deposition [31].

4.2 Cohesive and adhesive properties of GST films

Figure 4 presents the fracture strength of amorphous and crystalline GST as a function of film thickness. The fracture strength was calculated from fragmentation kinetics in the defect-controlled first regime (see Figure 2 (e)) in analogy to literature [32, 33]. Based on the weakest link model we assume that the fracture strength follows a two-parameter Weibull distribution. The strength distribution λ and k are obtained from linear approximation of the initial part of the crack distribution. The fracture strength is:

$$\boldsymbol{\sigma_f = \lambda\left(\frac{\overline{L}}{L_0}\right)^{-1/k}\Gamma(1+1/k) + \sigma_{res}} \qquad 2$$

Generally, amorphous films exhibit smaller fracture strength values than crystalline films. However, Figure 2 demonstrates that crystalline GST fractures at lower strains than amorphous GST. This apparent contradiction can be solved by considering that the Young's modulus of crystalline GST (E_f=30-40 GPa [12]) is two to four times larger than that of amorphous GST (E_f=10-20 GPa [12]) which results in a higher fracture strength of crystalline GST. The film thickness dependence of the fracture strength can be modeled according to Griffith's law ($\sigma_f \propto d^{-0.5}$). This law assumes that the dominant factor determining the fracture strength is defect growth throughout the film thickness d. Thicker films result in smaller fracture strength values because a larger film volume exhibits a higher number of ~~volume~~ defects. Consequently, the probability of critical defects at a certain stress is larger for thicker films.

In Figure 5 (a) the fracture toughness values K_{IC} of amorphous and crystalline GST are shown as a function of strain. These values were evaluated by the energy-based approach of a two-dimensional shear lag model derived by Frank *et al.* [34]. The energy release rate G

$\left(G = \sqrt{K_{IC}{}^{E_f}/(1-\nu_f^2)}\right)$ depends on the mean crack distance $\overline{L}$, the dimensionless parameter $\lambda = \xi/\overline{L}$ and the stress in tensile direction $\sigma_x = \frac{E_f \varepsilon}{1-\nu_f^2}(1 - \nu_f \nu_s) + \sigma_{res}$:

$$G = \frac{\overline{L}(1-\nu_f^2)}{E_f}\sigma_x^2\left[\frac{3\lambda sinh\left(\frac{1}{\lambda}\right) - 1}{2cosh^2\left(\frac{1}{2\lambda}\right)} - \frac{3\lambda sinh\left(\frac{2}{\lambda}\right) - 2}{4cosh^2\left(\frac{1}{\lambda}\right)}\right] \quad (3)$$

The stress transfer length $\xi = L_c/2$ is obtained from the critical length L_c which is related to L_{sat} the mean crack distance at saturation $L_c = 1.5 L_{sat}$ [32]. The Poisson's ratio of the substrate is assumed to be the same as that of Kapton® HN ($\nu_s = 0.34$) [35]. The model is valid in the strain regime $\varepsilon_c < \varepsilon < \varepsilon_b$, with ε_b the onset strain of delamination. For amorphous GST the model is applied in the strain regime $\varepsilon_c < \varepsilon < \varepsilon_{sat}$ as at strains beyond ε_{sat} no further cracks occur. For 200 nm and 400 nm GST films K_{IC} increases as a function of strain until it reaches a plateau value (see Figure 5 (a)). This strain-dependent evolution is expected as first cracks occur at the largest defects and consequently result in a reduced effective fracture toughness. The fracture toughness saturates at higher strain values as soon as the stress in the film reaches the fracture strength of the film. For 50 nm and 100 nm GST films this trend cannot be observed which might be due to uncertainties in the critical mean fragmentation length L_c. An error estimation indicates that a change in L_c has a minor influence on the calculated overall fracture toughness but changes the evolution of the fracture toughness as a function of strain. ~~Exemplarily, for~~ For each film thickness one error bar is plotted which ~~results~~ corresponds to the variation in ~~from uncertainties of in the~~ Young's ~~modulus~~ moduli as reported in literature [8, 10-12].

In Figure 5 (b) the K_{IC}-values obtained at ε_c and ε_b, or respectively ε_{sat} for the model of Frank *et al.* are compared to the values calculated by the model of Beuth [36]. This model relies on a linear elastic response of substrate and coating:

$$G = \frac{\pi \sigma_f^2 d}{2E_f} g(\alpha,\beta) \qquad 4$$

The non-dimensionalized integral of the crack opening displacements $g(\alpha,\beta)$ depends on the Dundurs' parameters α and β [36]. For both models the obtained values scatter but are independent of the film thickness which indicates that there is no plastic deformation in the films. For amorphous GST an average fracture toughness of $K_{IC} = 0.4 \pm 0.2$ MPa m$^{0.5}$ is obtained and for crystalline GST the value is $K_{IC} = 0.8 \pm 0.2$ MPa m$^{0.5}$. Compared to other thin brittle films with K_{IC} values around 1-5 MPa m$^{0.5}$ [29, 37] these values are small. These difference in K_{IC} values can be explained by the small Young's modulus of GST.

Polymers also exhibit small Young's moduli and reduced fracture toughness values, but due to their large strain to fracture they are extensively exploited as substrate materials for flexible electronic applications. Consequently, in some applications the criteria of maximum strain to fracture K_{IC}/E_f or maximum stored energy K_{IC}^2/E_f are more important. For flexible electronics e.g. the strain to fracture value is of prime importance as it describes the failure of the device. Comparing the strain to fracture values of GST (amorphous GST: K_{IC}/E_f=(30 ± 14)·10^{-6} m$^{0.5}$; crystalline GST: K_{IC}/E_f=(23 ± 6)·10^{-6} m$^{0.5}$) with those of Si (amorphous Si: K_{IC}/E_f=(18 ± 3)·10^{-6} m$^{0.5}$; crystalline Si: K_{IC}/E_f=(20 ± 8)·10^{-6} m$^{0.5}$) shows that the values are comparable and GST films even exhibit slightly larger maximum strains to fracture than Si.

4.3 Onset strain of fragmentation and delamination

To investigate the critical parameters of crack formation with respect to crystallography and geometry of the GST films, we compare the experimental and simulated strain-dependent RA spectra with results of the onset strains of fragmentation determined by ~~optical~~ light microscopy and resistance measurements.

The RAS method, as shown in the Figure 3, is very sensitive to monitor the onset of crack initiation under uniaxial deformation. From an optical perspective, the nucleated crack acts as a single subwavelength slit altering the interaction with the incoming electromagnetic field *E* [38]. Depending on the polarization of the electric field, the subwavelength slit will allow resonant coupling to the lowest order slit mode of the crack (TM, *E* perpendicular) or will behave as an effective medium (TE, *E* parallel). The resonant coupling can be understood as Fabry-Perot resonance, whereby the resonant condition depends on the film thickness [38].The numerically computed RA spectra reproduce the thickness-dependent shift of the RAS dip observed in our experiments (see Figure 3 (c) and 3 (d)), and fit well within in the framework of Fabry-Perot resonances in subwavelength slits.

With increasing strain, multiple cracks are nucleated until a state of stress relaxation is reached. Single subwavelength slits within this array can interact and form a grating resonance [39]. In analogy to transmission gratings, the overall electromagnetic response depends in general on the geometrical parameters of the slit array, which are crack distance, crack opening, and film thickness [40].

Figure 3 (f) presents the intensity value of Re($\Delta r/r$) at the respective energy value of the crack feature of amorphous GST as a function of strain. The films of all thicknesses first possess the

same linear change of the anisotropy signal behavior during loading which is attributed to film thinning. The strain value where the RA signal deviates from the linear behavior depends on the film thickness and is taken as onset strain of fragmentation. Thicker films start to deviate at lower strain values from the initial linear behavior than thinner films.

The reflectance anisotropy of crystalline GST was recorded at the photon energy of the elastic feature at 5.06 eV during continuous loading (see Figure 3 (g)). At low strains the films of all thicknesses exhibit a linear increase in intensity as a function of strain, which is perfectly reversible upon cyclic loading as presented for 30 nm crystalline GST. The initial slope of the RA signal of 30 nm crystalline GST differs from that of the other films which might be explained by different ratios of hexagonal and cubic phases (see Figure 1 (b)). The strain value where the signal starts to deviate from this linear behavior differs for each film thickness. It is taken as yield point where the elastic deformation stops.

A saturation of the RA signal at strains larger than the yield point corresponds to plastic deformation [16] and a decrease of the signal results from stress relaxation of the film due to crack formation. Here, the ~~decrease of the~~ RA signal decreases at strain values larger than the yield point which indicates that no plastic deformation occurs. The decrease of the RA signal is not only caused by stress relaxation but also by the overlying crack feature signal. That explains the qualitatively different curve shapes after the maximum for GST films of different film thickness in Figure 3 (g).

The RA feature at 5.06 eV can be attributed to the piezo-optic tensor and reflect critical points in the electronic band structure of crystalline GST. The electronic band structures of cubic and hexagonal GST were calculated in literature [41]. Both are complex and the authors were not able

to determine all critical points. Moreover, for cubic GST the results are based on calculations for the lowest energy structure where intrinsic vacancies are ordered. At real conditions they are randomly distributed in the material. Consequently, it is challenging to find a transition in the band structure which corresponds to the RA feature at 5.06 eV. However, numerous conductive bands around 5 eV [41] at the Γ-point and a high density of states at this energy [42] indicate that several transitions may be accessible. That would also explain that the RA signal at 5.06 eV is broader than usually observed for a single transition [16].

To demonstrate that the onset strains of fragmentation determined by RAS are reliable, we compare these strain values with the onset strain of fragmentation determined by ~~optical~~ light microscopy and resistance measurements. Figure 6 presents the results for amorphous (a) and crystalline (b) GST films. The values obtained by RAS are in excellent agreement with those of the two other methods which indicates that the method is reliable. Moreover, ~~optical~~ light microscopy and resistance measurements could not be used to determine the formation of cracks in 20 nm and 30 nm thin GST films while this was partly feasible for reflectance anisotropy spectroscopy.

A comparison of the onset strain of fragmentation of amorphous and crystalline GST (Figure 6 (a) and (b)) shows that crystalline GST starts to fracture at lower strains than amorphous GST which may origin from the larger residual tensile stress of crystalline GST.

The RAS measurements support the interpretation of the resistance measurement of crystalline GST: The difference in slope of the normalized resistance change compared to the ideal resistance change at low strains in Figure 2 (d) cannot be explained by small intrinsic cracks which open upon straining because besides the resistance measurements also the RA feature at 5.06 eV is perfectly

reversible at low strain values which demonstrates that it corresponds to elastic deformation. From the slope of the initial resistance curves in Figure 2 (d) a piezoresistive gauge factor of $GF = \Delta R/R\varepsilon^{-1} =$ 10-20 is calculated which is in the same order of magnitude as that of polycrystalline Si ($GF = \pm$ 30) but much smaller than p-type silicon with $GF =$ 200 [43].

Figure 7 presents the onset strain of delamination of crystalline GST determined by ~~optical~~ light microscopy. The delamination behavior follows the strain energy criterion $\varepsilon_b \propto d^{-0.5}$ where thinner films delaminate at higher strains than thicker films [44]. The fit of the onset strain of delamination as a function of film thickness is shown in Figure 7.

Amorphous GST does not exhibit any delamination up to a strain of 20 %. This observation is in good agreement with scratch tests of amorphous and crystalline GST which indicate that the adhesion of amorphous GST films is enhanced compared to that of crystalline GST [45].

5. Conclusion

We have investigated the mechanical properties of amorphous and crystalline $Ge_2Sb_2Te_5$ (GST) films in the film thickness range from 20 nm to 400 nm by uniaxial tensile tests. In particular, we have studied the cohesive and adhesive properties of GST films, which is a key criterion when GST is applied as reflective coating or temperature sensor on flexible substrates.

Mechanical properties: The maximum strain to fracture of GST is similar to that of Si. Si is heavily exploited for flexible electronics, which makes GST a promising candidate for flexible display applications with substrate materials that are thin enough to be bent. It has been shown that the mechanical properties of GST can be significantly enhanced by reducing the film thickness. However, due to their brittle nature stretching of GST films should be prevented.

Electrical properties: Quite interestingly, resistance measurements of crystalline GST revealed a piezoresistive effect upon straining which is in the same order of magnitude as that of polycrystalline Si. This effect may need to be considered for display applications on flexible substrates. Switching a GST film between its amorphous and crystalline phase is typically induced by electrical Joule heating. A larger resistance of a GST layer due to an applied tensile strain will result in slightly more Joule heating for a given current density.

Methods: It was further demonstrated that RAS is a reliable tool to determine the onset strain of fragmentation for materials which exhibit straight and parallel cracks. Moreover, RAS measurements in combination with finite element simulations indicate that GST is a promising material for subwavelength grating where the slit width and grating period can be tuned by uniaxial loading.

6. Acknowledgement

The authors thank the FIRST Center for Micro- and Nanoscience at ETH Zurich for the possibility to use the sputter tool. They gratefully acknowledge T. Weber for performing the XRD measurement of crystalline GST at the X-ray platform, Department of Materials, ETH Zurich. F.S. thanks R. Denk and P. Zeppenfeld for fruitful discussions about the RAS data. A.W. acknowledges funding by the Helmholtz Gemeinschaft in the form of Helmholtz Virtual Institute VI530. H.G. gratefully acknowledges financial support from the “Size Matters!” project, (TDA Capital, UK).

Figure captions:

Figure 1: (a) The XRD scan of 400 nm crystalline GST exhibits peaks of fcc and hcp reflections. (b) Raman spectra of amorphous and crystalline GST films are clearly distinguishable. The peaks of 30 nm crystalline GST are larger than those of 100 nm crystalline GST which indicates that the ratio of fcc and hcp is different for 30 nm GST.

Figure 2: Optical micrographs of crack patterns of 100 nm amorphous (a) and crystalline (b) GST at various strains are presented. The cracks are perpendicular to the loading direction. In contrast to amorphous GST, crystalline GST exhibits delamination at 18 % strain. Normalized resistance versus strain for (c) amorphous GST films with 3 nm conductive Pt top layers and (d) crystalline GST films. The black solid lines correspond to the ideal resistance change in the elastic strain regime while the dashed lines indicate a 5 % deviation from this ideal behavior. ~~Exemplarily,~~ Typically, reversible loading and unloading curves are presented for (d) 30 nm crystalline GST at low strain values. Mean crack distance as a function of strain of amorphous (e) and crystalline (f) GST films. The three crack regimes are plotted for 100 nm amorphous GST (e).

Figure 3: Measured RA spectra of 100 nm amorphous (a) and crystalline (b) GST at various strain values. A feature at 2.80 eV is clearly visible for amorphous and crystalline GST which is dubbed the crack feature in the following. Crystalline GST (b) exhibits another feature at 5.06 eV which is called the elastic feature. Measurement (c) and simulation (d) of RA spectra of 50 nm, 100 nm, and 400 nm amorphous GST. The spectral position of the crack feature depends on the film thickness and is highlighted with a dashed line for each film thickness. For the simulation constant crack openings of 80 nm and crack distances of 970 nm are assumed (e). Evolution of the RA signals of amorphous (f) and crystalline (g) GST films as a function of strain. Reversible loading and unloading curves are presented for 30 nm crystalline GST (g).

Figure 4: Fracture strength values as a function of film thickness of amorphous and crystalline GST are presented. The error bars result from uncertainties of the Young's moduli. Griffith's law ($\boldsymbol{\sigma_f \propto d^{-0.5}}$) is fitted to the data.

Figure 5: (a) Fracture toughness $\boldsymbol{K_{IC}}$ plotted as a function of strain for amorphous and crystalline GST determined by the model introduced by Frank *et al.* (b) The $\boldsymbol{K_{IC}}$-values obtained by the model of Frank *et al.* and Beuth are plotted as a function of film thickness. Generally, crystalline GST is tougher than amorphous GST.

Figure 6: Thickness-dependent onset strain of fragmentation of amorphous (a) and crystalline (b) GST films determined by RAS, ~~optical~~ light microscopy, and resistance measurements. For comparison the onset strain of fragmentation of 500 nm amorphous GST determined by Choi *et al.* [11] is included.

Figure 7: Onset strain of delamination of crystalline GST determined by ~~optical~~ light microscopy. The data is fitted by the strain energy criterion.

[1] M. Wuttig, N. Yamada. Phase-change materials for rewriteable data storage, Nat Mater 6 (2007) 824-832.
[2] K. Shportko, S. Kremers, M. Woda, D. Lencer, J. Robertson, M. Wuttig. Resonant bonding in crystalline phase-change materials, Nat Mater 7 (2008) 653-658.
[3] W. Wełnic, M. Wuttig. Reversible switching in phase-change materials, Materials Today 11 (2008) 20-27.
[4] S.R. Ovshinsky. Reversible Electrical Switching Phenomena in Disordered Structures, Physical Review Letters 21 (1968) 1450-1453.

[5] Y. Chen, X. Li, Y. Sonnefraud, A.I. Fernández-Domínguez, X. Luo, M. Hong, S.A. Maier. Engineering the Phase Front of Light with Phase-Change Material Based Planar lenses, Scientific Reports 5 (2015) 8660.

[6] P. Hosseini, C.D. Wright, H. Bhaskaran. An optoelectronic framework enabled by low-dimensional phase-change films, Nature 511 (2014) 206-211.

[7] F.F. Schlich, P. Zalden, A.M. Lindenberg, R. Spolenak. Color Switching with Enhanced Optical Contrast in Ultrathin Phase-Change Materials and Semiconductors Induced by Femtosecond Laser Pulses, ACS Photonics 2 (2015) 178-182.

[8] T.P.L. Pedersen, J. Kalb, W.K. Njoroge, D. Wamwangi, M. Wuttig, F. Spaepen. Mechanical stresses upon crystallization in phase change materials, Applied Physics Letters 79 (2001) 3597-3599.

[9] V. Weidenhof, I. Friedrich, S. Ziegler, M. Wuttig. Atomic force microscopy study of laser induced phase transitions in Ge2Sb2Te5, Journal of Applied Physics 86 (1999) 5879-5887.

[10] I.-M. Park, J.-K. Jung, S.-O. Ryu, K.-J. Choi, B.-G. Yu, Y.-B. Park, S.M. Han, Y.-C. Joo. Thermomechanical properties and mechanical stresses of Ge2Sb2Te5 films in phase-change random access memory, Thin Solid Films 517 (2008) 848-852.

[11] Y. Choi, Y.-K. Lee. Elastic modulus of amorphous Ge2Sb2Te5 thin film measured by uniaxial microtensile test, Electronic Materials Letters 6 (2010) 23-26.

[12] Y. Won, J. Lee, M. Asheghi, T.W. Kenny, K.E. Goodson. Phase and thickness dependent modulus of Ge2Sb2Te5 films down to 25 nm thickness, Applied Physics Letters 100 (2012) 161905.

[13] P. Weightman, D.S. Martin, R.J. Cole, T. Farrell. Reflection anisotropy spectroscopy, Reports on Progress in Physics 68 (2005) 1251.

[14] D.E. Aspnes, J.P. Harbison, A.A. Studna, L.T. Florez. Application of reflectance difference spectroscopy to molecular-beam epitaxy growth of GaAs and AlAs, Journal of Vacuum Science & Technology A 6 (1988) 1327-1332.

[15] M. Hohage, L.D. Sun, P. Zeppenfeld. Reflectance difference spectroscopy – a powerful tool to study adsorption and growth, Applied Physics A 80 (2005) 1005-1010.

[16] A. Wyss, M. Schamel, A.S. Sologubenko, R. Denk, M. Hohage, P. Zeppenfeld, R. Spolenak. Reflectance anisotropy spectroscopy as a tool for mechanical characterization of metallic thin films, Journal of Physics D: Applied Physics 48 (2015) 415303.

[17] D. Papadimitriou, W. Richter. Highly sensitive strain detection in silicon by reflectance anisotropy spectroscopy, Physical Review B 72 (2005) 075212.

[18] R.J. Cole, S. Kheradmand, D.D. Higgins, F. Madani, B.F. Macdonald, V. Koutsos, J.R. Blackford. Stress-induced optical anisotropy in polycrystalline copper studied by reflection anisotropy spectroscopy, Journal of Physics D: Applied Physics 36 (2003) L115.

[19] Y. Choi, M. Jung, Y.-K. Lee. Effect of Heating Rate on the Activation Energy for Crystallization of Amorphous Ge2Sb2Te5 Thin Film, Electrochemical and Solid-State Letters 12 (2009) F17-F19.

[20] G.G. Stoney. The Tension of Metallic Films Deposited by Electrolysis, Proceedings of the Royal Society of London A: Mathematical, Physical and Engineering Sciences 82 (1909) 172-175.

[21] S. Frank. Determination of Crack and Buckle Density by Digital Image Analysis. MathWorks, 2008.

[22] O. Acher, B. Drévillon. A reflectance anisotropy spectrometer for real-time measurements, Review of Scientific Instruments 63 (1992) 5332-5339.

[23] T. Zhang, B. Liu, J.-L. Xia, Z.-T. Song, S.-L. Feng, B. Chen. Structure and Electrical Properties of Ge2Sb2Te5 Thin Film Used for Ovonic Unified Memory, Chinese Physics Letters 21 (2004) 741.

[24] N. Lu, Z. Suo, J.J. Vlassak. The effect of film thickness on the failure strain of polymer-supported metal films, Acta Materialia 58 (2010) 1679-1687.

[25] R.E. Simpson, M. Krbal, P. Fons, A.V. Kolobov, J. Tominaga, T. Uruga, H. Tanida. Toward the Ultimate Limit of Phase Change in Ge2Sb2Te5, Nano Letters 10 (2010) 414-419.

[26] T. Kato, K. Tanaka. Electronic Properties of Amorphous and Crystalline Ge2Sb2Te5 Films, Japanese Journal of Applied Physics 44 (2005) 7340.

[27] Y. Sun, S.E. Thompson, T. Nishida. Physics of strain effects in semiconductors and metal-oxide-semiconductor field-effect transistors, Journal of Applied Physics 101 (2007) 104503.
[28] A.A. Barlian, W.T. Park, J.R. Mallon, A.J. Rastegar, B.L. Pruitt. Review: Semiconductor Piezoresistance for Microsystems, Proceedings of the IEEE 97 (2009) 513-552.
[29] S. Frank, P.A. Gruber, U.A. Handge, R. Spolenak. In situ studies on the cohesive properties of α- and β-Ta layers on polyimide substrates, Acta Materialia 59 (2011) 5881-5892.
[30] A.S. Alagoz, J.-D. Kamminga, S.Y. Grachev, T.-M. Lu, T. Karabacak. Residual Stress Reduction in Sputter Deposited Thin Films by Density Modulation, MRS Online Proceedings Library Archive 1224 (2009) 1224-FF1205-1222 (1226 pages).
[31] K.L. Mittal. Adhesion Aspects of Thin Films, CRC Press Taylor and Francis Group, 2005.
[32] G. Rochat, Y. Leterrier, P. Fayet, J.A.E. Månson. Mechanical analysis of ultrathin oxide coatings on polymer substrates in situ in a scanning electron microscope, Thin Solid Films 437 (2003) 204-210.
[33] Y. Leterrier, L. Boogh, J. Andersons, J.A.E. Månson. Adhesion of silicon oxide layers on poly(ethylene terephthalate). I: Effect of substrate properties on coating's fragmentation process, Journal of Polymer Science Part B: Polymer Physics 35 (1997) 1449-1461.
[34] S. Frank, U.A. Handge, S. Olliges, R. Spolenak. The relationship between thin film fragmentation and buckle formation: Synchrotron-based in situ studies and two-dimensional stress analysis, Acta Materialia 57 (2009) 1442-1453.
[35] DuPont. Kapton HN data sheet. 2011.
[36] J.L. Beuth. Cracking of thin bonded films in residual tension, International Journal of Solids and Structures 29 (1992) 1657-1675.
[37] F.F. Schlich, R. Spolenak. Size- and phase-dependent mechanical properties of ultrathin Si films on polyimide substrates, Acta Materialia 110 (2016) 122-130.
[38] R. Gordon. Light in a subwavelength slit in a metal: Propagation and reflection, Physical Review B 73 (2006) 153405.
[39] J. Zhou, L.J. Guo. Transition from a spectrum filter to a polarizer in a metallic nano-slit array, Scientific Reports 4 (2014) 3614.
[40] J.A. Porto, F.J. García-Vidal, J.B. Pendry. Transmission Resonances on Metallic Gratings with Very Narrow Slits, Physical Review Letters 83 (1999) 2845-2848.
[41] J.-W. Park, S.H. Eom, H. Lee, J.L.F. Da Silva, Y.-S. Kang, T.-Y. Lee, Y.H. Khang. Optical properties of pseudobinary GeTe, Ge2Sb2Te5, GeSb2Te4, GeSb4Te7, and Sb2Te3 from ellipsometry and density functional theory, Physical Review B 80 (2009) 115209.
[42] S. Liu, J. Wei, F. Gan. Optical nonlinear absorption characteristics of crystalline Ge2Sb2Te5 thin films, Journal of Applied Physics 110 (2011) 033503.
[43] S.E. Beeby, G.; Kraft, M.; White, N. MEMS Mechanical Sensors, Artech House, INC, 2004.
[44] H.H. Yu, M.Y. He, J.W. Hutchinson. Edge effects in thin film delamination, Acta Materialia 49 (2001) 93-107.
[45] L. Yanbo, Z. Ting, Z. Guoxin, N. Xiaoming, S. Zhitang, M. Guoquan, L. Yun, Z. Jing, Z. Weimin, Z. Jianping, C. Jiangtao, W. YongZhong, F. Songlin. Study on Adhesive Strength between Ge2Sb2Te5 Film and Electrodes for Phase Change Memory Application, Japanese Journal of Applied Physics 48 (2009) 101601.

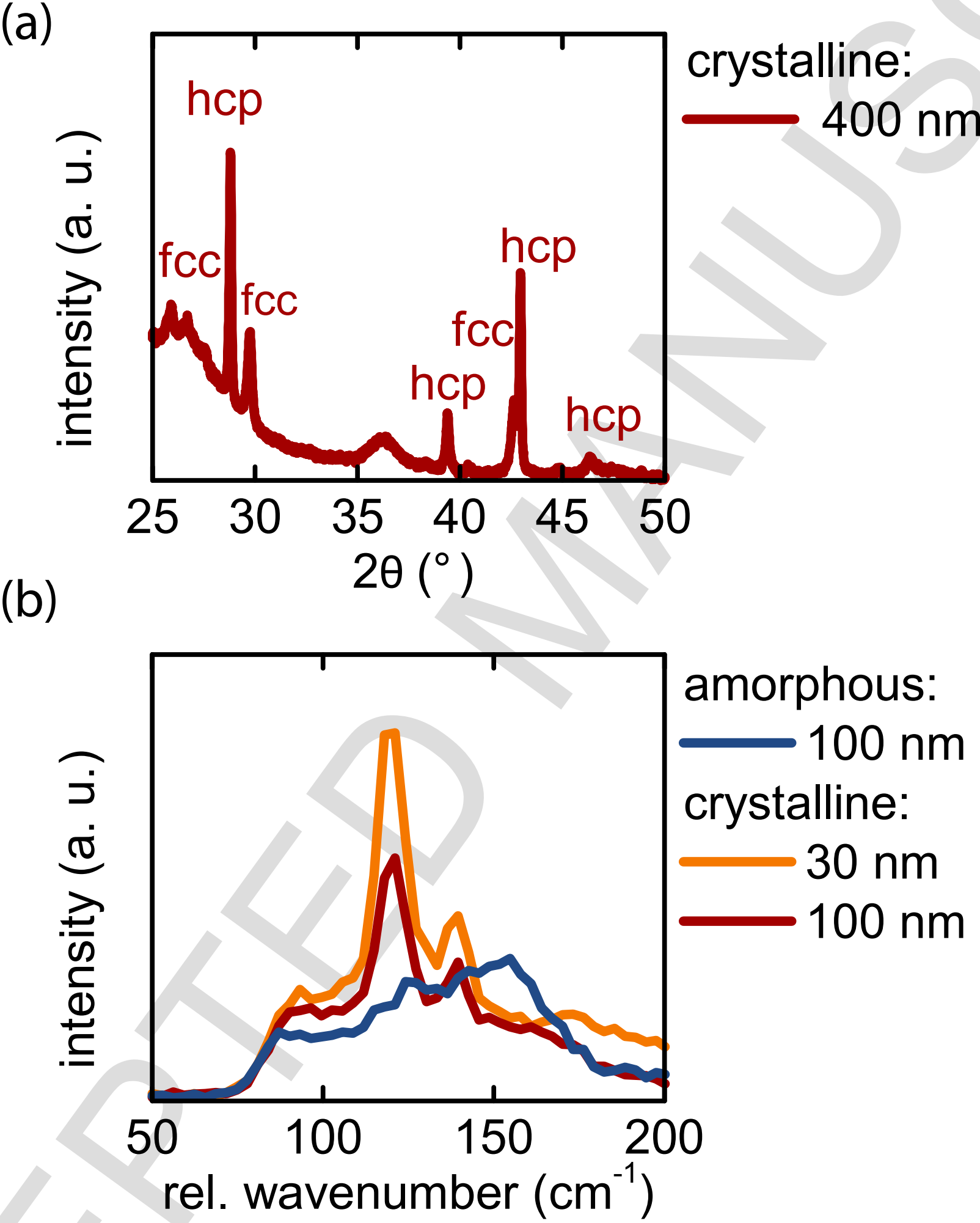
(a)
hcp
fcc
fcc
hcp
fcc
hcp
intensity (a. u.)
25
30
35
40
45
50
2θ (°)
crystalline:
400 nm
(b)
intensity (a. u.)
50
100
150
200
rel. wavenumber (cm-1)
amorphous:
100 nm
crystalline:
30 nm
100 nm

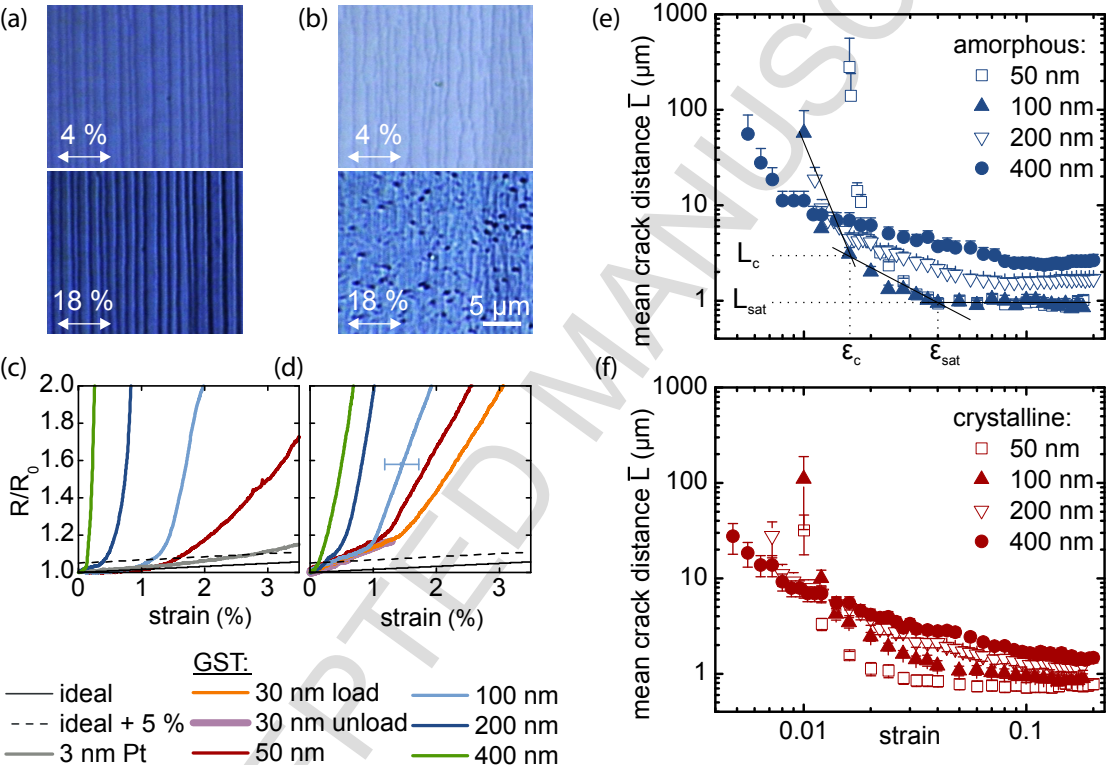
(a)
4 %
18 %
(b)
4 %
18 %
5 µm
(c)
R/R0
strain (%)
(d)
strain (%)
(e)
mean crack distance L̄ (µm)
amorphous:
50 nm
100 nm
200 nm
400 nm
Lc
Lsat
εc
εsat
(f)
mean crack distance L̄ (µm)
crystalline:
50 nm
100 nm
200 nm
400 nm
strain
GST:
ideal
ideal + 5 %
3 nm Pt
30 nm load
30 nm unload
50 nm
100 nm
200 nm
400 nm

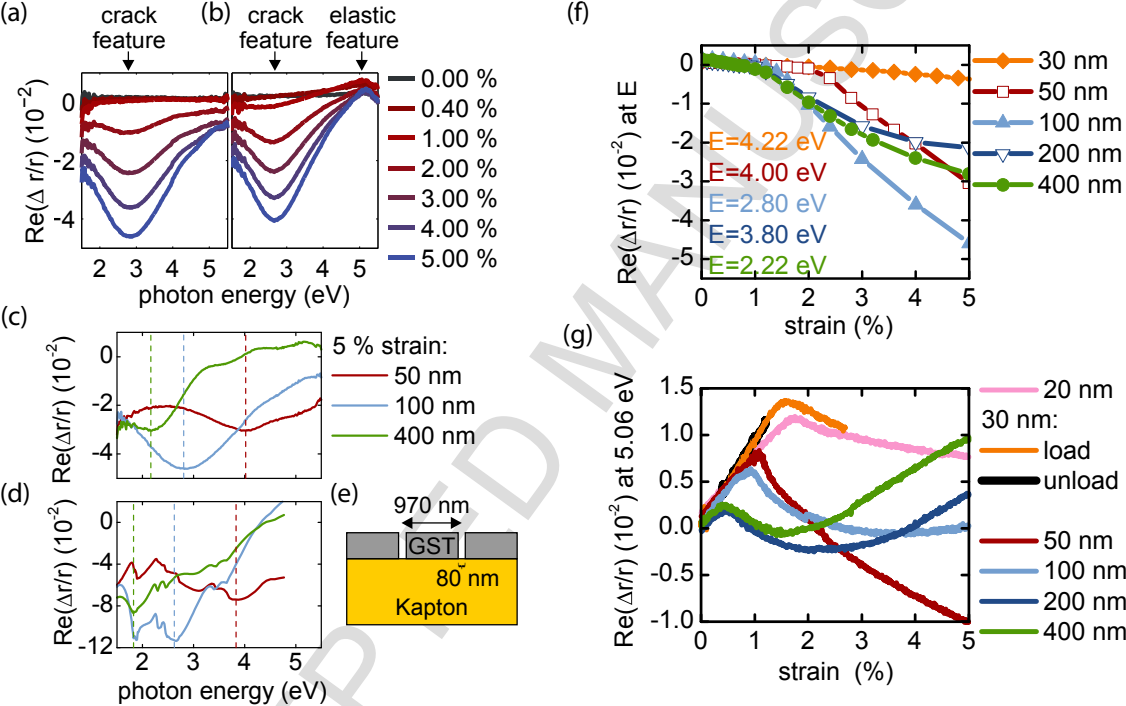
(a)
crack feature
(b)
crack feature
elastic feature
Re(Δ r/r) (10^{-2})
0
-2
-4
2 3 4 5
2 3 4 5
photon energy (eV)
0.00 %
0.40 %
1.00 %
2.00 %
3.00 %
4.00 %
5.00 %
(c)
Re(Δr/r) (10^{-2})
0
-2
-4
5 % strain:
50 nm
100 nm
400 nm
(d)
Re(Δr/r) (10^{-2})
0
-4
-8
-12
2 3 4 5
photon energy (eV)
(e)
970 nm
GST
80 nm
Kapton
(f)
Re(Δr/r) (10^{-2}) at E
0
-1
-2
-3
-4
-5
E=4,22 eV
E=4.00 eV
E=2.80 eV
E=3.80 eV
E=2,22 eV
0 1 2 3 4 5
strain (%)
30 nm
50 nm
100 nm
200 nm
400 nm
(g)
Re(Δr/r) (10^{-2}) at 5.06 eV
1.5
1.0
0.5
0.0
-0.5
-1.0
0 1 2 3 4 5
strain (%)
20 nm
30 nm:
load
unload
50 nm
100 nm
200 nm
400 nm

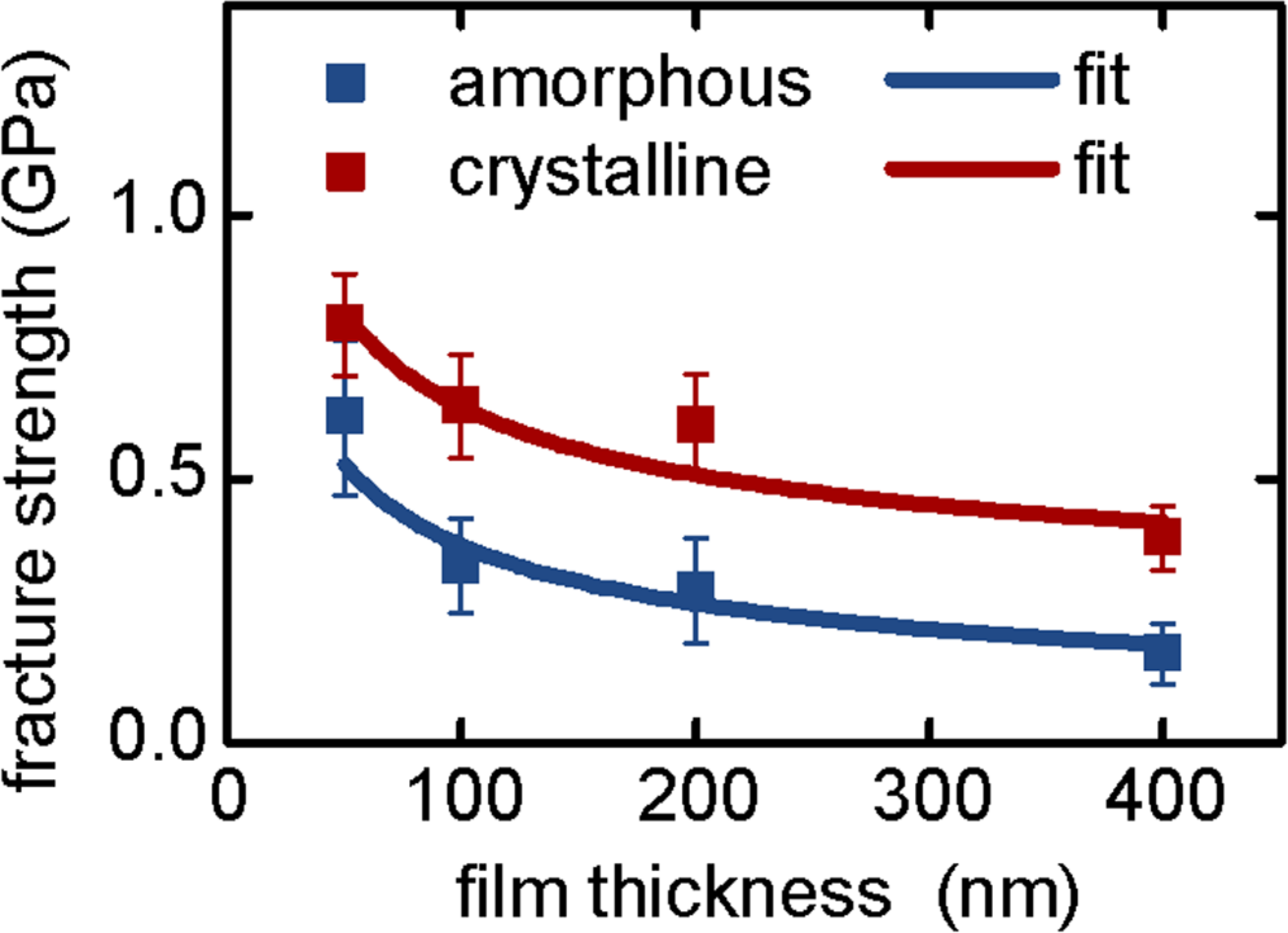
amorphous
crystalline
fit
fit
fracture strength (GPa)
1.0
0.5
0.0
0
100
200
300
400
film thickness (nm)

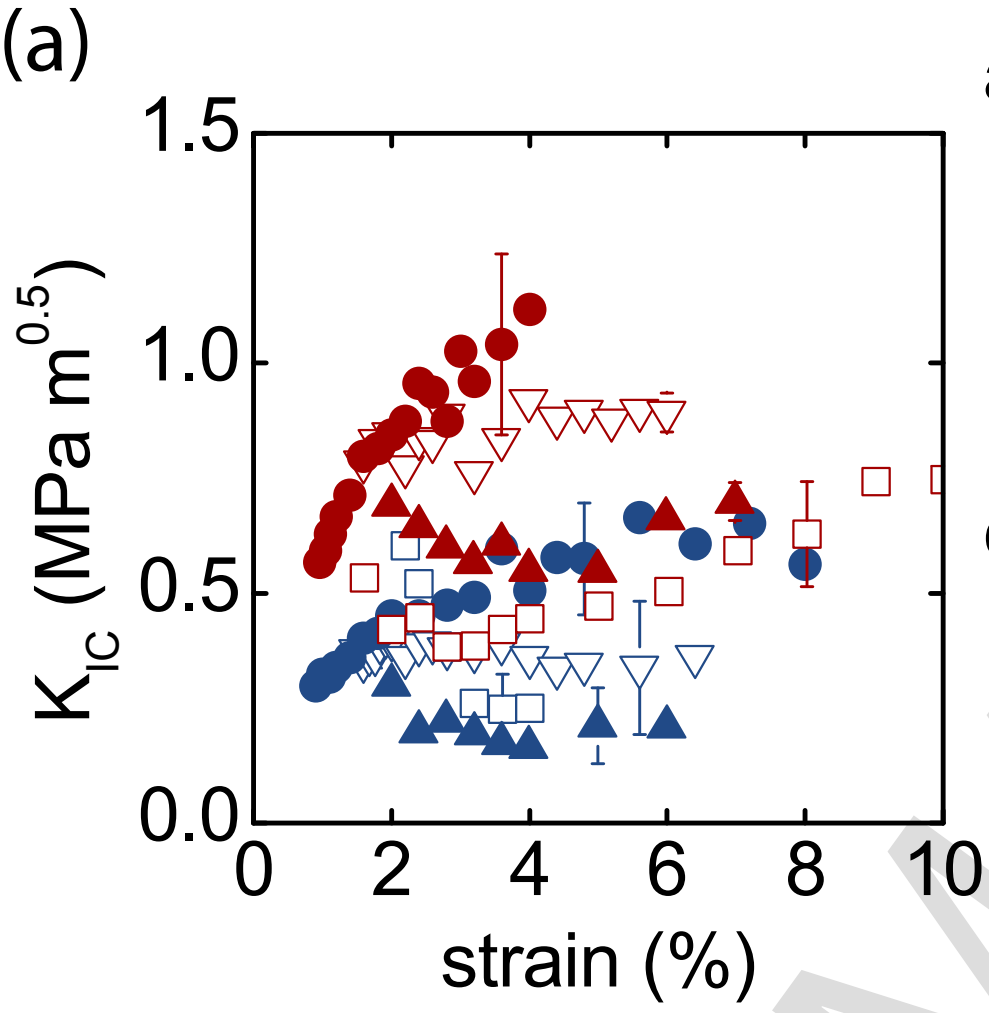

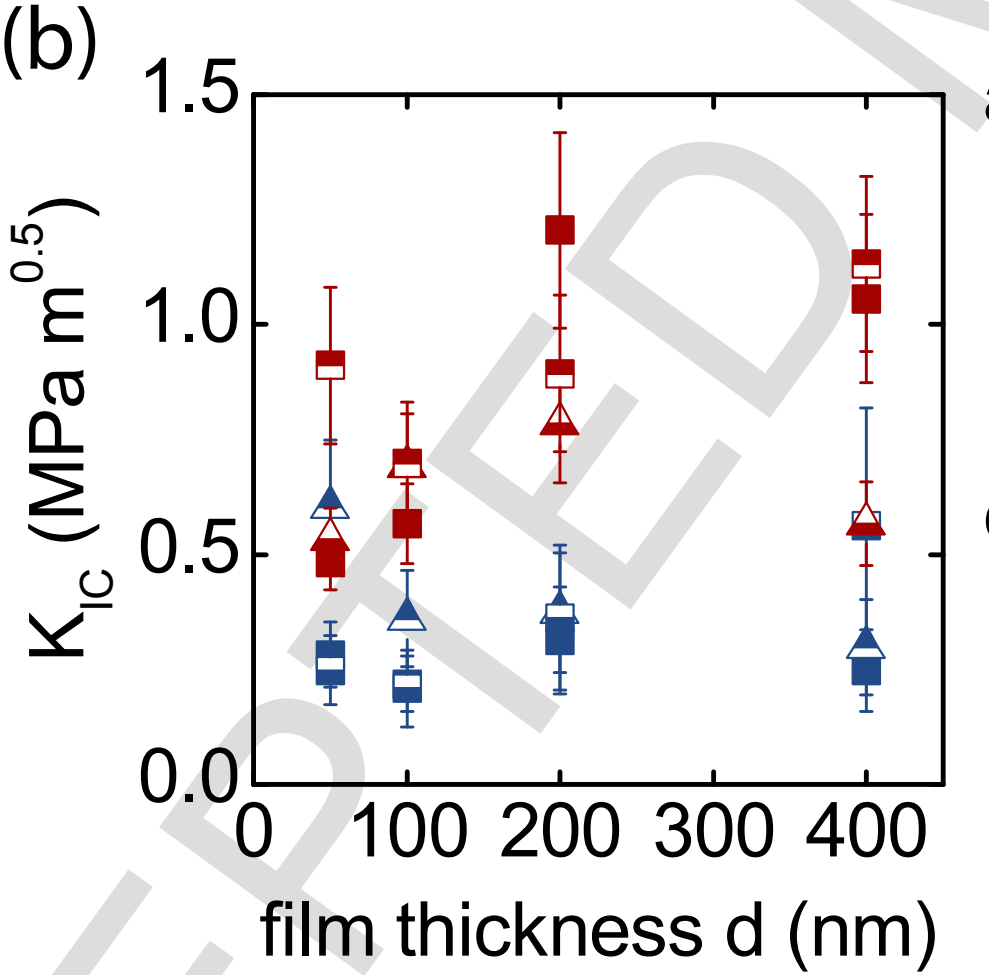

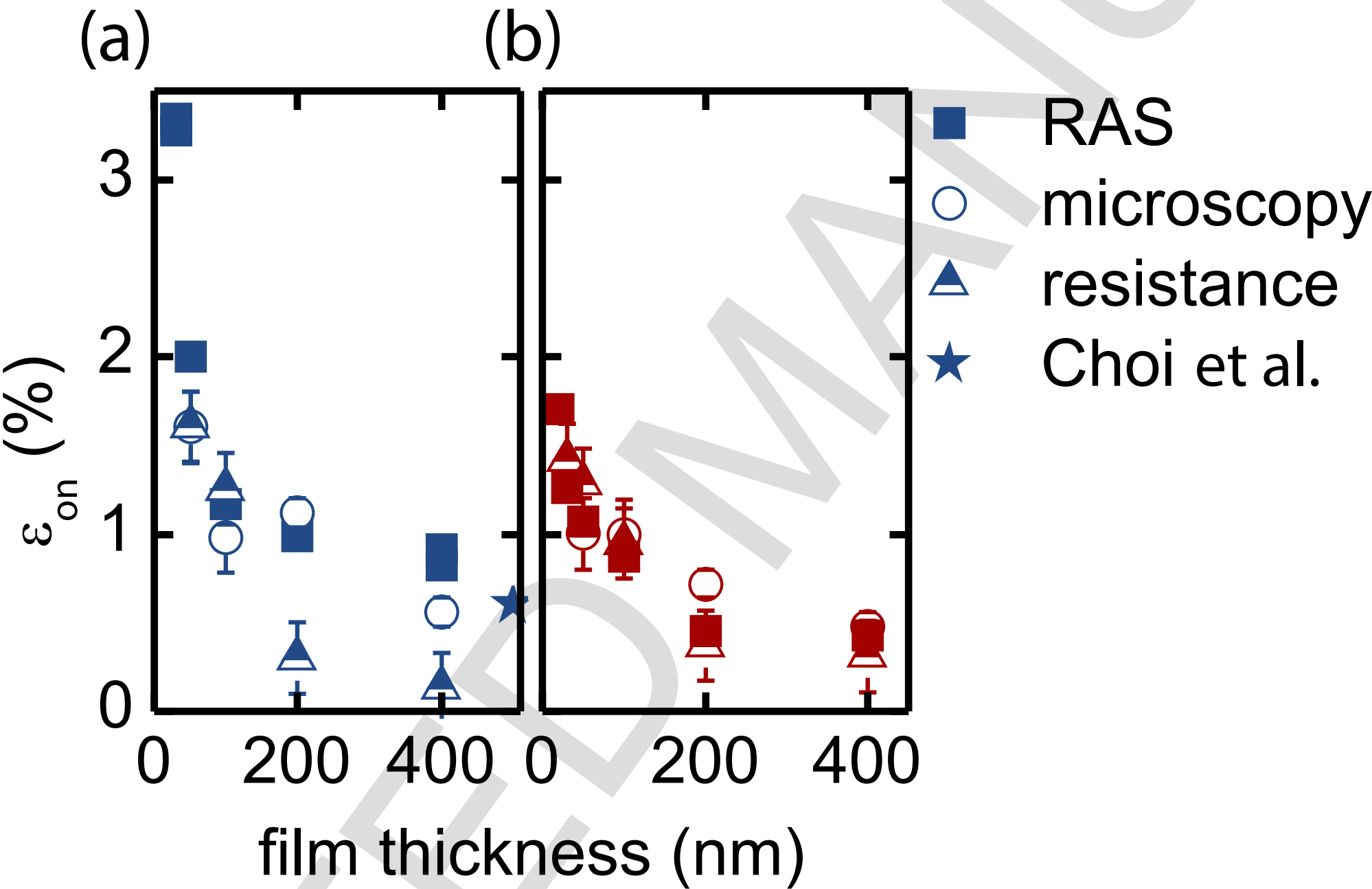
(a)
(b)
RAS
microscopy
resistance
Choi et al.
ε_{on} (%)
0
1
2
3
0
200
400
0
200
400
film thickness (nm)

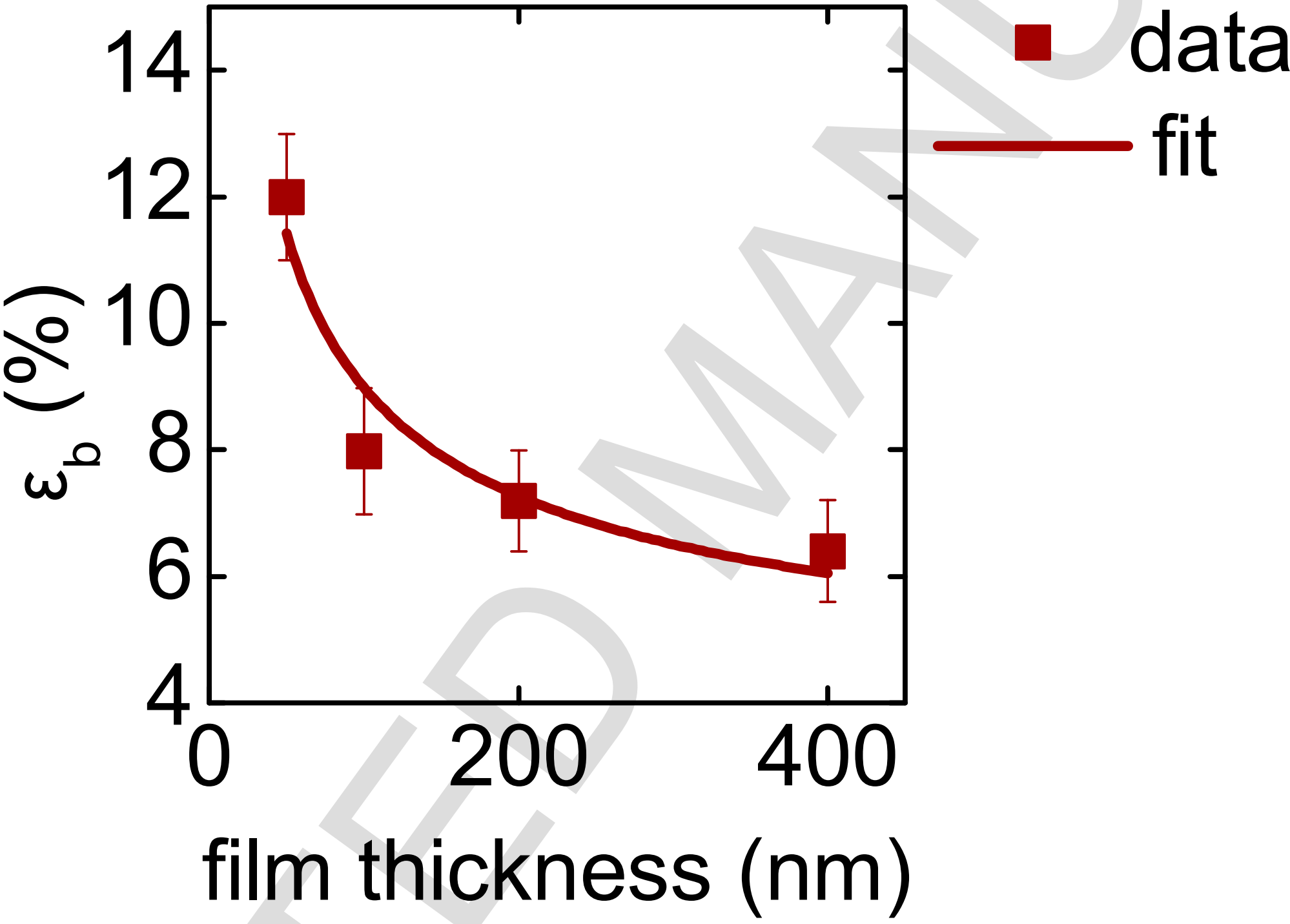
14
12
10
8
6
4
0
200
400
ε_b (%)
film thickness (nm)
data
fit

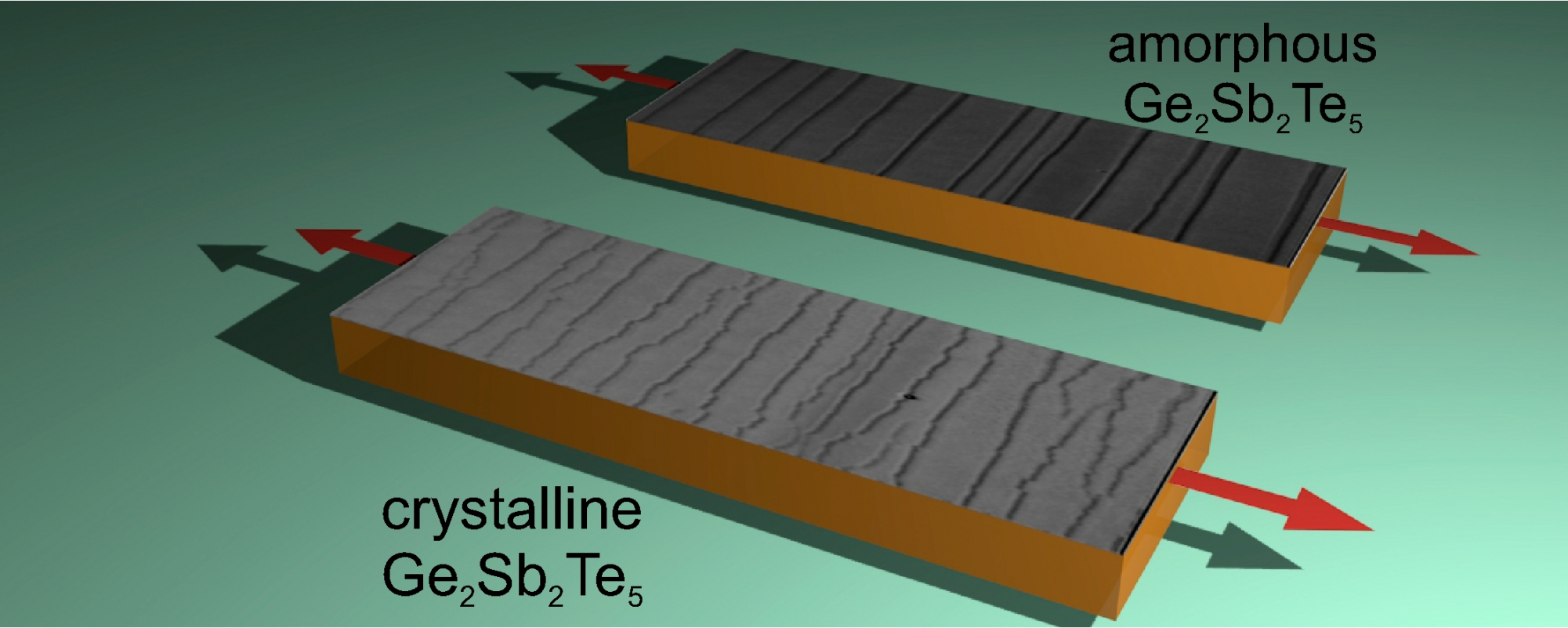
amorphous
$Ge_2Sb_2Te_5$
crystalline
$Ge_2Sb_2Te_5$